Phosphorus fuels *Cladophora* growth and self-reinforcing adhesion via extracellular polysaccharides on hard substrata

Supplementary Information

Yifan Du[a,c,#] Siguang Yuan[b,#] Jinyi Qin[c] Siming Jiao[d] Yufan Ai[a,g] Yingjie Li[a,g] Nan Li[b] Xiaonan Chen[b,e,f] Xiaoming Cai[d] Xinzong Xiao[b,e,f,*] Jilong Wang[a] Min Yang[a,g] Ming Su[a,g,*]

[#] These authors contributed equally to this work.

[a] Key Laboratory of Environmental Aquatic Chemistry, State Key Laboratory of Regional Environment and Sustainability, Research Center for Eco-Environmental Sciences, Chinese Academy of Sciences, Beijing 100085, China.

[b] China South to North Water Diversion Middle Route Corporation Limited, Beijing 100038, China.

[c] School of Civil Engineering, Chang'an University, Xi'an 710064, China.

[d] Institute of Process Engineering, Chinese Academy of Sciences, Beijing 100190, China.

[e] Hubei Key Laboratory of Intelligent Monitoring, Early Warning and Protection for Watershed Aquatic Ecology, Wuhan 430010, China.

[f] Water Quality and Aquatic Ecosystem Observation and Research Station of South-to-North Water Diversion Middle Line Project, Beijing 100038, China.

[g] University of Chinese Academy of Sciences, Beijing 100049, China.

[*] Corresponding to: Xinzong Xiao (xiaoxinzong@csnwd.com.cn), Ming Su (mingsu@rcees.ac.cn)

Figures and/or tables are provided below as the supplementary evidences to the main text.

Table of contents

Supplementary data

S1.1 Preparation of EPS films

Total EPS obtained as described in Section 2.3 was redissolved at 1 mg mL^{-1}[1]. An aliquot of the EPS solution was drop-cast onto freshly cleaved mica disks (12 mm in diameter and 0.1 mm in thickness) and allowed to dry naturally at room temperature to form a continuous film. Independently extracted EPS samples were deposited on separate mica disks and treated as biological replicates. Before force-spectroscopy measurements, the dried EPS films were mounted in the AFM liquid cell and hydrated with PBS (pH 7.4) at approximately 25 °C. This film-based configuration was used throughout; EPS was not immobilized on the probe surface.

S1.2 Probe selection and calibration

RTESPA-150 probes were used for topographic imaging of the dried EPS films, whereas BL-AC40TS Si_3N_4 probes were used for force-spectroscopy measurements and the chemical-perturbation experiments. The inverse optical lever sensitivity was determined from the linear contact region of force–distance curves acquired on a rigid mica surface under the corresponding measurement conditions. The cantilever spring constant was subsequently determined from the thermal-noise spectrum. The calibrated inverse optical lever sensitivity and spring constant were 82 nm V^{-1} and 6.0 N m^{-1}, respectively, for RTESPA-150 probes, and 20 nm V^{-1} and 0.10 N m^{-1}, respectively, for BL-AC40TS probes. The thermal-noise procedure provides an independent calibration of cantilever stiffness from its thermally driven fluctuations.

S1.3 Stepwise disruption of EPS polysaccharide structures

Matched EPS films prepared from the same EPS batch were used to distinguish the contribution of the intact polysaccharide framework from that of glucuronic-acid-containing domains. Native EPS films were first measured as untreated controls.

For polysaccharide-backbone disruption, an aliquot of the extracted total EPS was hydrolyzed with 1 mol L^{-1} TFA at 121 °C for 2 h. After hydrolysis, TFA was removed by evaporation under a nitrogen stream, and the residue was redissolved in ultrapure water at 1 mg mL^{-1}. The hydrolyzed EPS solution was subsequently drop-cast onto freshly cleaved mica disks and dried under the same conditions as the untreated EPS to prepare matched films for force-spectroscopy measurements.

Following TFA treatment, β-glucuronidase solution was introduced directly into the AFM liquid cell. A 100 μL aliquot of enzyme solution was added to obtain an activity of 1 U mL^{-1}, and force–distance curves were collected after 5, 10, and 20 min of in situ incubation. This additional enzymatic treatment was used to evaluate the involvement of residual glucuronic-acid-containing domains associated with acidic polysaccharides. The native, TFA-treated, and subsequently enzyme-digested states were compared under otherwise identical liquid-phase measurement conditions.

The relative loss of adhesion following TFA hydrolysis was calculated as:

$$R_{\mathrm{TFA}} = \frac{F_{\mathrm{native}} - F_{\mathrm{TFA}}}{F_{\mathrm{native}}} \times 100\%$$

where Fnative and FTFAare the mean adhesion forces of the untreated and TFA-treated EPS films, respectively. The resulting percentage represents the proportion of measured adhesion lost after disruption of the polysaccharide framework and was not interpreted as a directly quantified mass contribution of polysaccharides. The additional decrease following β-glucuronidase digestion was calculated as:

$$\Delta F_{\beta\text{-GUS}} = F_{\mathrm{TFA}} - F_{\mathrm{TFA}+\beta\text{-GUS}}$$

and was used to assess the additional involvement of glucuronic-acid-containing domains in residual EPS-mediated adhesion.

Supplementary Methods S2. EPS-associated extractable phosphorus (EPS-P)

Water-column TP and SRP were measured to characterize the background phosphorus conditions of the *Cladophora* growth environment. Phosphorus associated with canal-slope sediments was determined to represent the bulk P pool accumulated at the algal–substratum interface. In parallel, an aliquot of the EPS extract was analyzed to quantify phosphorus co-extracted with the extracellular matrix. A procedural blank containing identical extraction reagents but no algal material was processed in parallel, and the blank value was subtracted from the corresponding EPS-extract measurement. A phosphate-free extraction control with comparable pH and ionic strength was additionally included. The corrected fraction is hereafter termed EPS-associated extractable phosphorus (EPS-P).

Supplementary Methods S3. Determination and blank correction of EPS-associated extractable phosphorus

An aliquot of the combined EPS extract was collected before ethanol precipitation for phosphorus determination. A procedural blank containing the same types and volumes of extraction buffers and reagents, but without algal material, was processed through the complete EPS extraction and analytical procedure in parallel with each sample batch. The phosphorus concentration measured in the procedural blank was subtracted from that measured in the corresponding EPS extract: CEPS−P=CEPS extract−Cprocedural blank. A matched phosphate-free extraction system with comparable pH and ionic strength was used to verify that the EPS-P signal was not attributable to phosphate introduced by the extraction medium. EPS-P was expressed as mg kg^{-1} and operationally defined as the phosphorus pool co-extracted with the extracellular matrix.

Supplementary Methods S4. EPS-mediated adhesion

EPS-mediated adhesion should be interpreted as stabilizing attachment-layer establishment and biomass retention during the substrate-associated stage, rather than permanently anchoring individual filaments throughout the vegetation cycle. As the attached biomass matured, hydraulic

disturbance and seasonal senescence could promote detachment, after which filamentous material entered the drifting phase and was transported downstream as filament–particle aggregates. Thus, canal-scale persistence reflected sustained or recurrent occupation of favorable wall habitats at the population level, while individual filaments could transition from attached to drifting states.

Supplementary Fig. 1

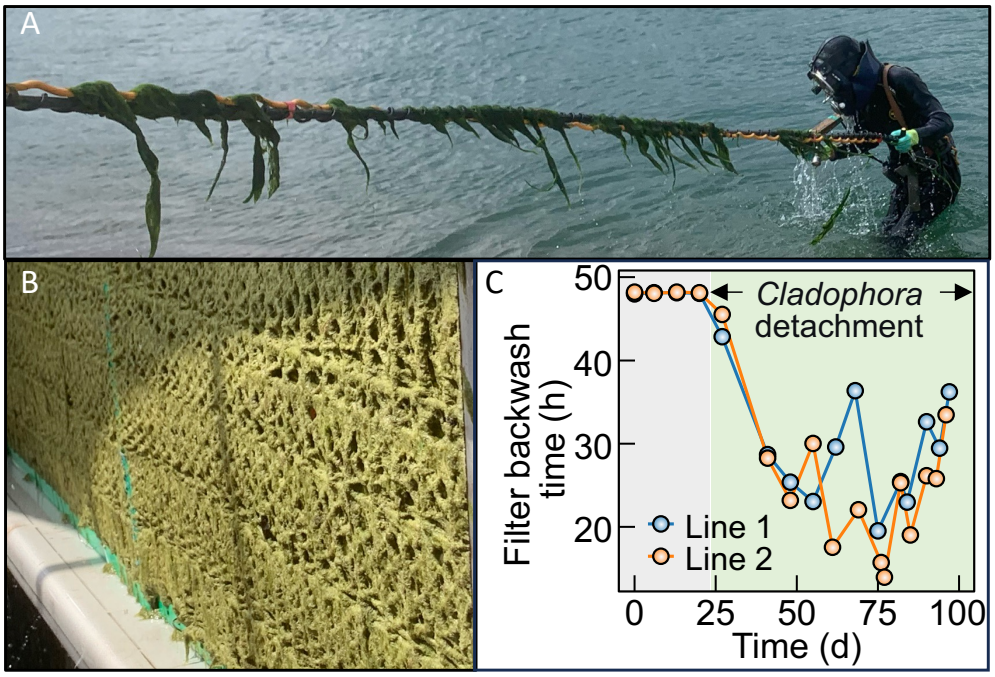

Supplementary Fig. 1: *Cladophora* in the conveyance canal and associated engineering impacts. (A) The longest *Cladophora* filament harvested by diver (~1 m). (B) Mesh-like biofilm morphology comprising algal filaments and EPS matrix attached to canal walls and filter media surfaces. (C) Progressive shortening of rapid sand-filter backwash cycles attributed to *Cladophora* attachment (Lines 1 and 2 denote independent filter units) and detachment dynamics.

Supplementary Fig. 2

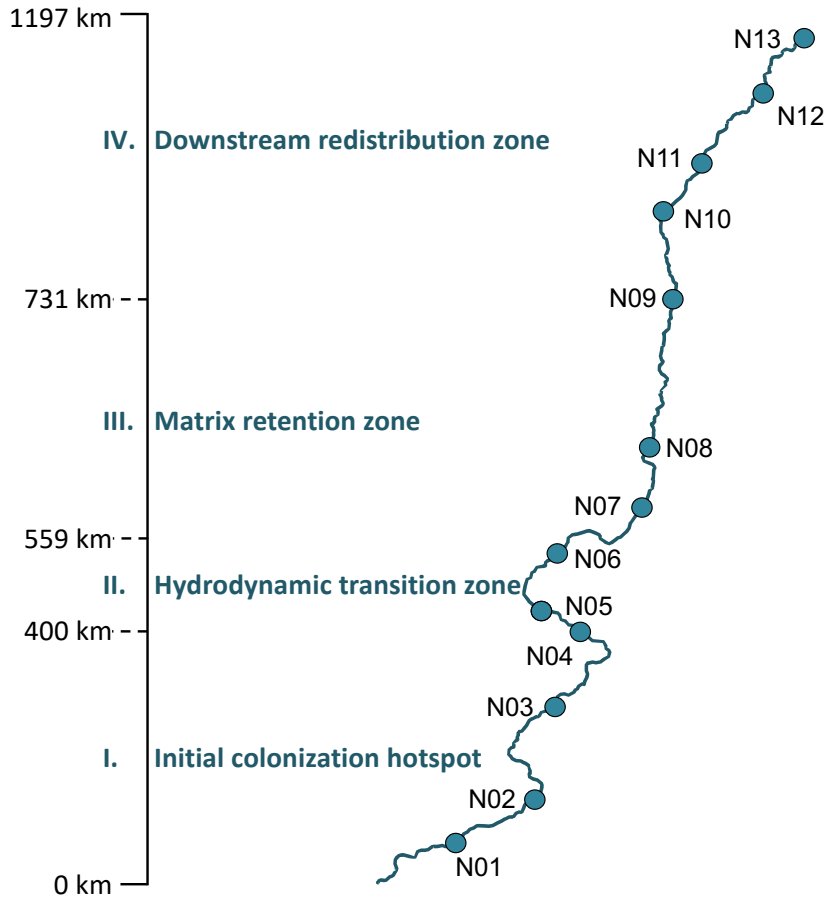

Supplementary Fig. 2: Sampling sites of this study along the study transect.

Supplementary Table 1

Ingredients	Content	Unit
Water temperature	28.16±2.24	℃
pH	8.35±0.20	—
DO	8.23±0.56	mg L^{-1}
COD_{Mn}	1.99±0.21	mg L^{-1}
COD	7.43±1.64	mg L^{-1}
BOD_5	0.73±0.39	mg L^{-1}
NH_4^+-N	0.045±0.022	mg L^{-1}
TP	6.59±2.67	μg L^{-1}
TN	1.06±0.11	mg L^{-1}
SO_4^{2-}	25.29±1.27	mg L^{-1}

Supplementary Table 1: Summary of the main water quality parameters in the study area during July–August (2022–2024). Values are presented as mean±standard deviation. DO, COD_{Mn}, COD, BOD_5, NH_4^+-N, TN, and SO_4^{2-} are reported in mg L^{-1}, whereas TP is reported in μg L^{-1}. The dash indicates a dimensionless parameter. Data are expressed as mean ± standard deviation (n = 3).

Supplementary Fig. 3

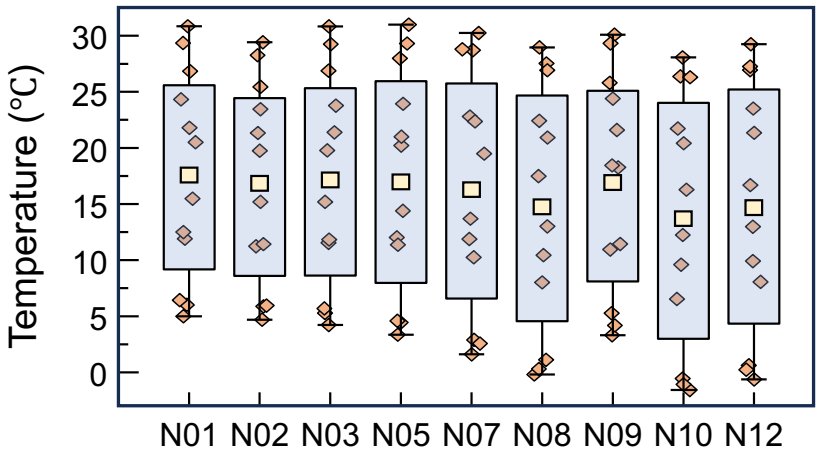

Supplementary Fig. 3: Sites N01–N09 are arranged from south to north. Overall, temperature exhibited pronounced seasonal variability across all sites, with an annual range of approximately 0–31°C. Spatially, the annual mean temperature generally decreased from about 18°C at the southern site N01 to about 15°C at the northern sites, indicating a northward declining temperature gradient. Notably, N09 showed a relatively higher annual mean temperature of approximately 20°C, deviating from the overall south-to-north decreasing trend and suggesting potential local environmental or hydrological influences.

Supplementary Fig. 4

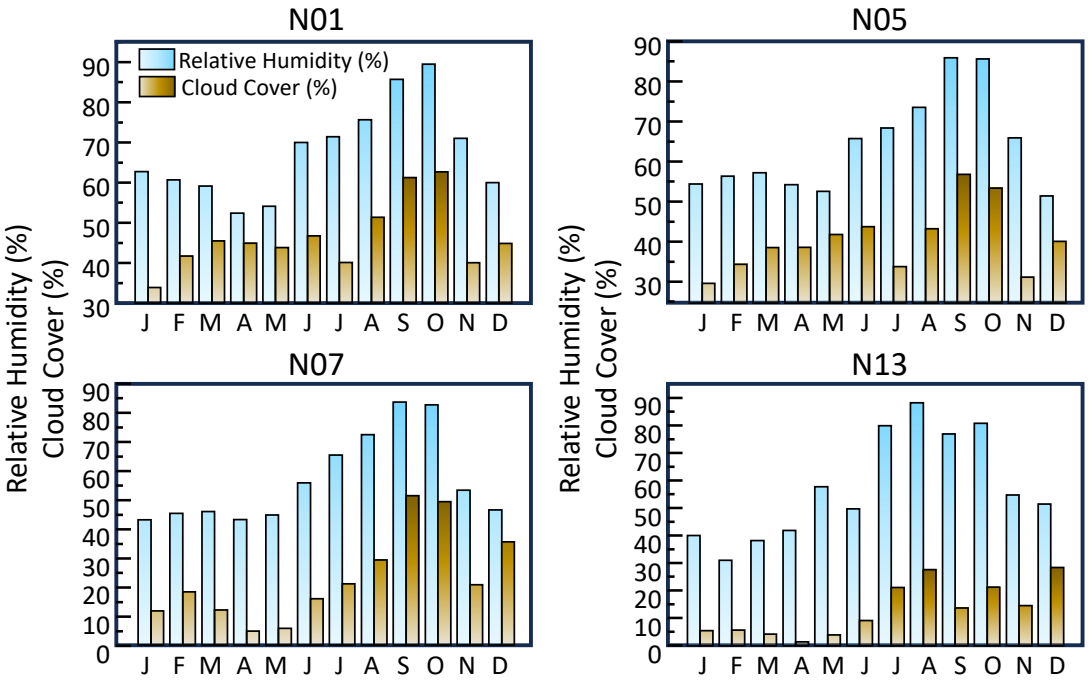

Supplementary Fig. 4: Monthly variations in relative humidity and cloud cover at representative sampling sites along the study transect in 2025. (A) N01, (B) N05, (C) N07, and (D) N13. Bars represent monthly relative humidity and cloud cover. Relative humidity and cloud cover showed broadly synchronous seasonal increases during the warm and wet period, whereas precipitation exhibited stronger episodic fluctuations.

Supplementary Fig. 5

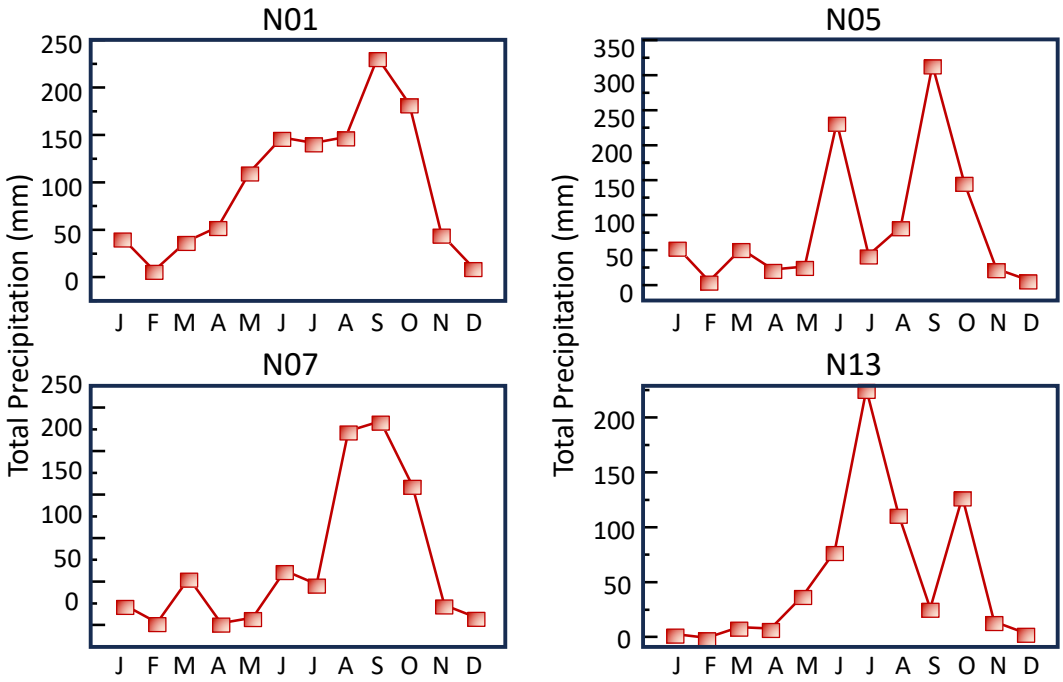

Supplementary Fig. 5: Monthly variations in total precipitation at representative sampling sites along the study transect in 2025. (A) N01, (B) N05, (C) N07, and (D) N13. Precipitation exhibited stronger episodic fluctuations. Precipitation peaks occurred mainly in September at N01, N05, and N07, but shifted to July at N13 with a secondary increase in October, indicating spatial heterogeneity in wet-season timing along the transect.

Supplementary Fig. 6

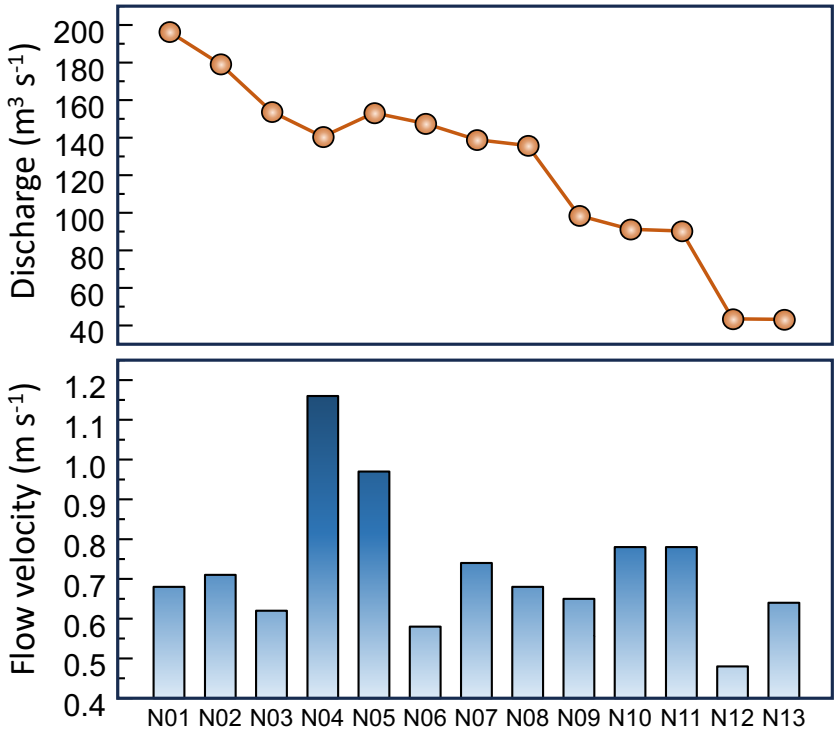

Supplementary Fig. 6: Longitudinal variation in flow velocity and discharge along the sampling transect. Flow velocity and discharge were measured from N01 to N13. Discharge showed an overall downstream decrease, from approximately 195 $m^3 s^{-1}$ at N01 to 40–45 $m^3 s^{-1}$ at N12–N13, with a local rebound at N05. Flow velocity varied among sites, ranging from approximately 0.48 to 1.16 $m s^{-1}$. The maximum velocity occurred at N04, whereas N12 showed the lowest velocity. N13 maintained low discharge but showed a slight recovery in flow velocity compared with N12.

Supplementary Fig. 7

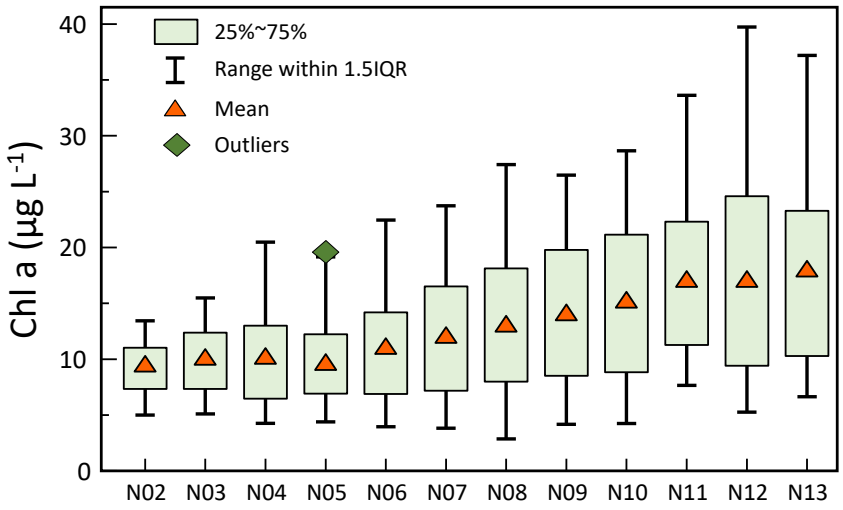

Supplementary Fig. 7: Longitudinal distribution of chlorophyll *a* concentrations across sampling sites. Chlorophyll *a* concentrations were summarized by box plots from N02 to N13. The median values remained within approximately 8 ~ 10 μg L^{-1} at N02–N07 and increased to approximately 12 ~ 17 μg L^{-1} at N08–N13. Mean concentrations increased from approximately 9–10 μg L^{-1} at N02–N05 to approximately 17–18 μg L^{-1} at N11–N13. The upper whiskers reached approximately 34–40 μg L^{-1} at N11–N13. A single outlier of approximately 19–20 μg L^{-1} was recorded at N05, exceeding the 1.5 IQR range for each site.

Supplementary Fig. 8

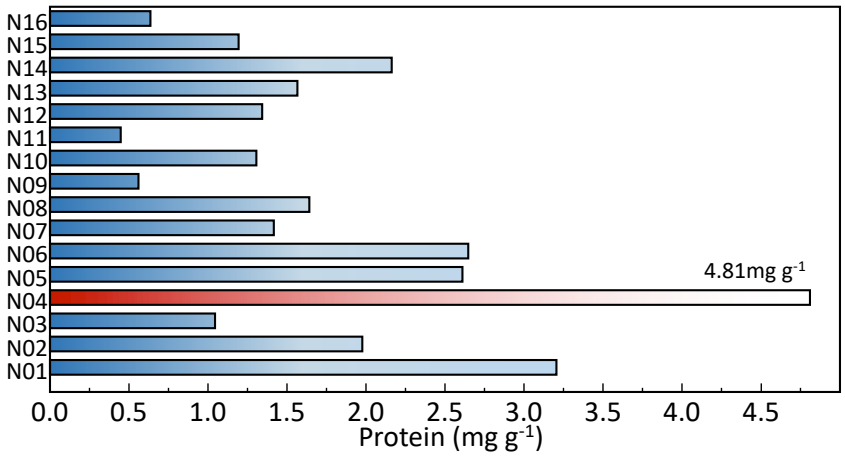

Supplementary Fig. 8: Longitudinal distribution of EPS-associated protein content in canal-slope sediment–biofilm matrices at 30 cm depth. Bars denote protein contents normalized to the dry mass of scraped sediment–biofilm matrices and expressed as mg g^{-1}. The highlighted N04 section showed the highest protein content, reaching 4.81 mg g^{-1}, indicating localized enrichment of proteinaceous extracellular materials at the 30 cm attachment-active layer.

Supplementary Fig. 9

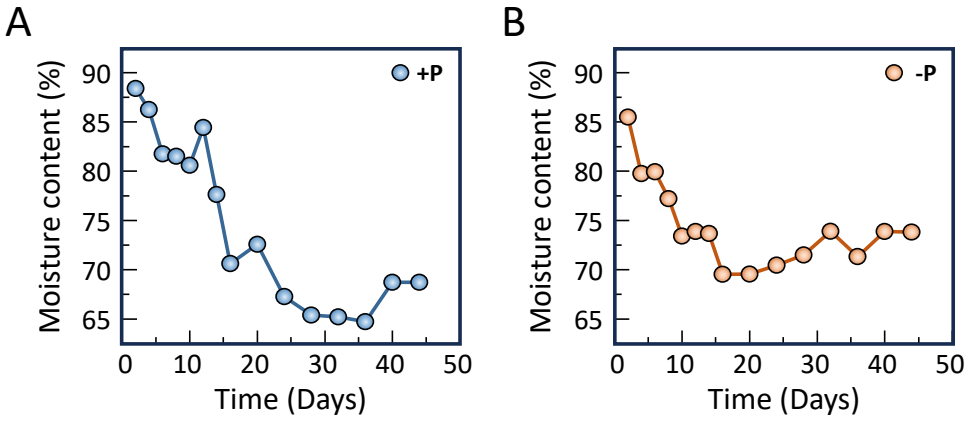

Supplementary Fig. 9: Moisture-content variation of laboratory-cultured *Cladophora* during the phosphorus-enrichment experiment. Moisture content of *Cladophora* initially inoculated at 0.5 g fresh weight under +P conditions (A); Moisture content of *Cladophora* initially inoculated at 0.5 g fresh weight under −P conditions. Moisture content was calculated from the mass loss after oven drying relative to the initial wet mass at each sampling point. The variation in moisture content indicates that fresh weight alone may not accurately reflect biomass accumulation during laboratory culture; therefore, dry-weight normalization was used for EPS and APS yield calculations.

Supplementary Fig. 10

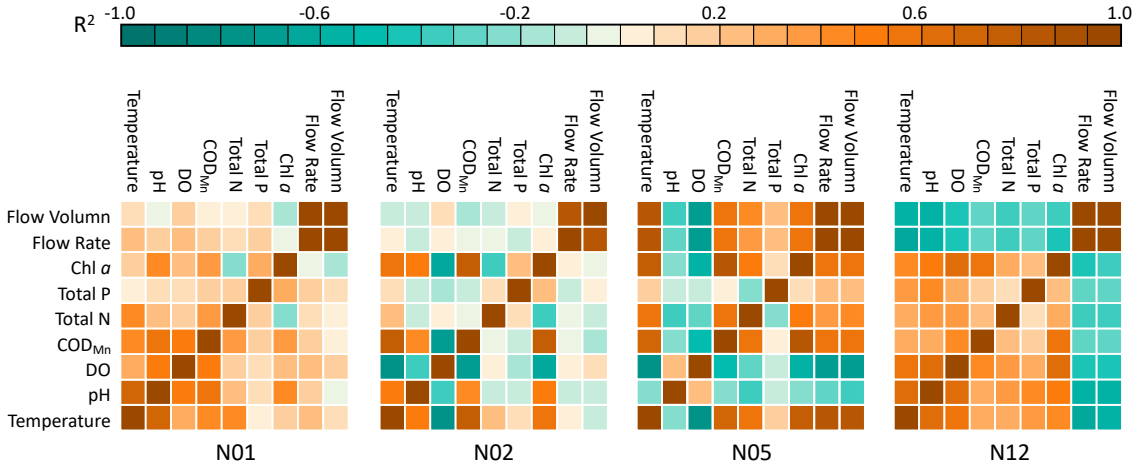

Supplementary Fig. 10: Site-specific correlation matrices among hydrological, physicochemical, and algal biomass variables at representative sampling sites. Pairwise correlations were calculated for N01, N05, N09, and N12. The variables include water temperature, pH, DO, COD_{Mn}, total nitrogen (Total N), total phosphorus (Total P), chlorophyll *a* (Chl *a*), flow velocity, and flow volume. Cell values represent correlation coefficients, with the color scale ranging from −1 to 1. Flow velocity and flow volume showed consistently positive correlations across the four sites, with coefficients of 0.800–0.987. Site-specific correlation structures were recorded: N01 showed positive correlations among temperature, pH, DO, and COD_{Mn}; N05 showed negative correlations between temperature and DO and between DO and CODMn; N09 showed positive correlations of temperature with COD_{Mn}, Chl *a*, flow velocity, and flow volume; and N12 showed negative correlations of flow velocity and flow volume with temperature, pH, and Chl *a*.

Supplementary Table 2

Predictor	Estimate	Standard error	t value	P value	Significance
CODMn	12.876	1.567	8.215	<0.001	***
Temperature	1.987	0.298	6.668	<0.001	***
Flow velocity	-8.765	8.987	-0.975	0.333	ns
DO	-0.567	0.876	-0.647	0.520	ns
TN	-6.234	4.123	-1.512	0.136	ns
TP	-23.456	56.789	-0.413	0.681	ns
pH	2.345	2.567	0.913	0.365	ns
Discharge	0.012	0.045	0.267	0.790	ns

Supplementary Table 2: Regression coefficients of environmental predictors at site N06. Estimates, standard errors, t values, and P values were derived from the regression model for site N06. COD_{Mn}, permanganate index; DO, dissolved oxygen; TN, total nitrogen; TP, total phosphorus. Flow velocity and discharge are expressed as m s^{-1} and m^3 s^{-1}, respectively. Significance levels are denoted as *** $p<0.001$ and ns, not significant.

Supplementary Fig. 11

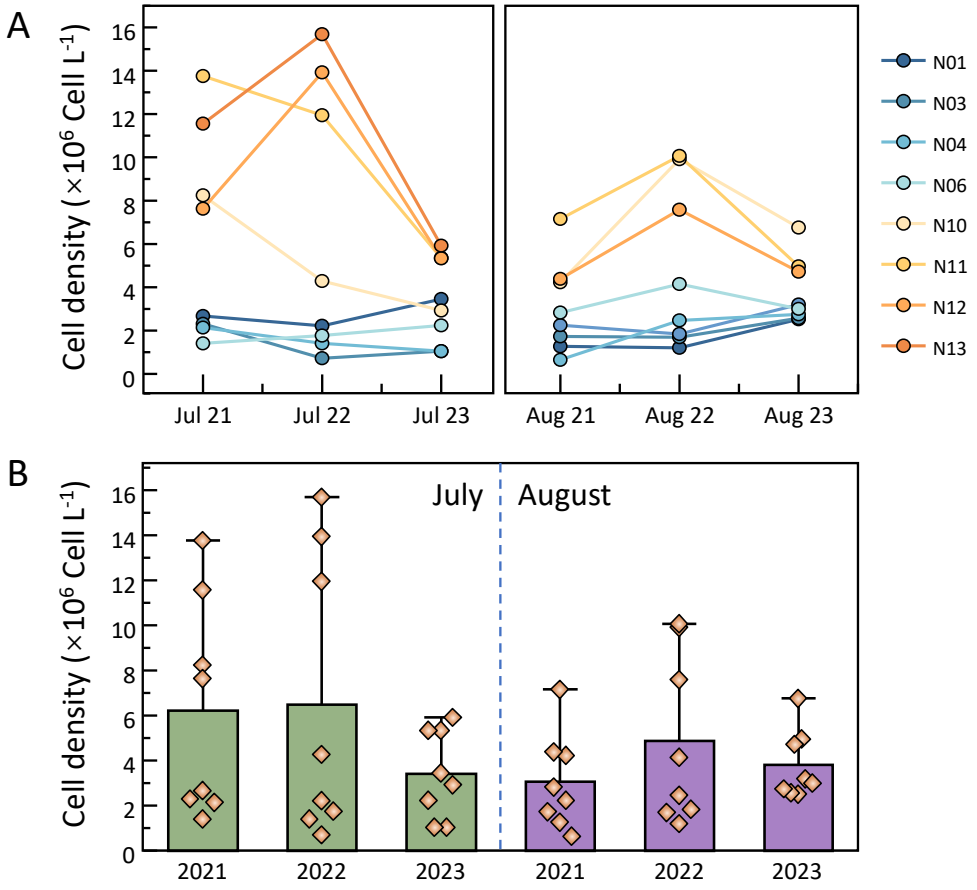

Supplementary Fig. 11: Temporal and spatial variation in phytoplankton density at representative sampling sites during July and August from 2021 to 2023. Phytoplankton density was compared among N01, N03, N04, N06, N10, N11, N12, and N13, with July and August separated by the dashed vertical line. Densities at N01, N03, N04, and N06 were generally within 0.6 ~ 4.2×10^6 cell L^{-1}, whereas N10–N13 showed wider interannual fluctuations. The highest value occurred at N13 in July 2022, reaching approximately 1.560 × 10^7 cell L^{-1}, followed by N11 in July 2022 and N10 in July 2021. In August, the maximum densities were recorded in 2022 at N10 and N11, both approaching 1.000 × 10^7 cell L^{-1}. The inset summarizes the among-site distribution of plankton density for each sampling month.

Supplementary Fig. 12

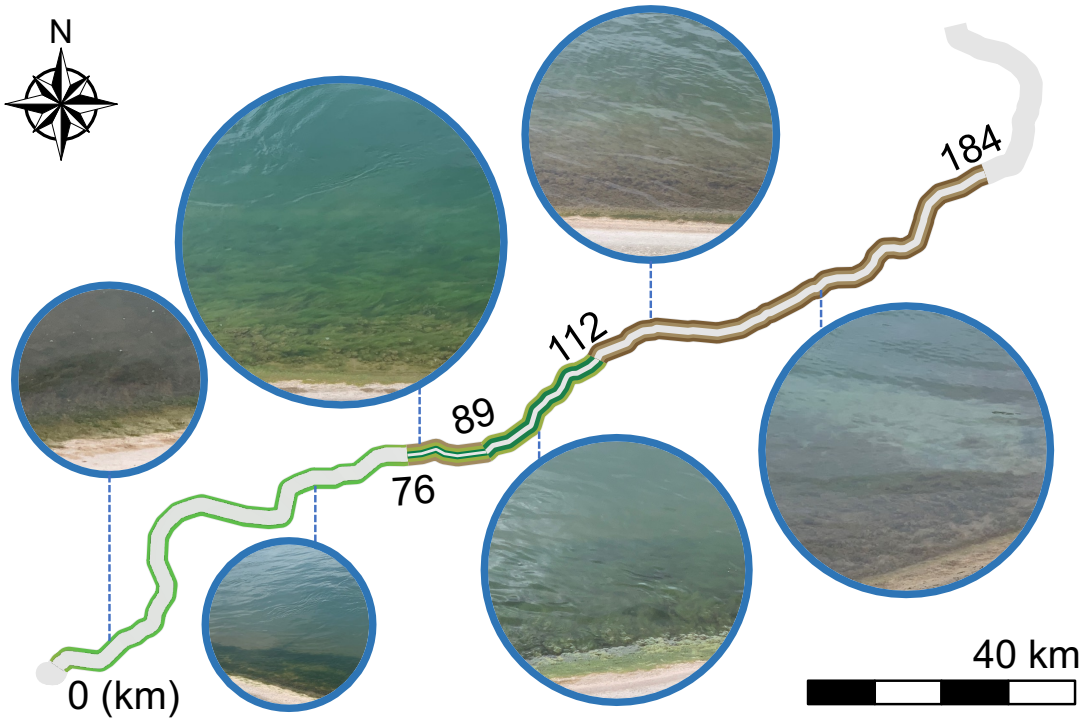

Supplementary Fig. 12: Spatial distribution of *Cladophora* in the conveyance canal. Variations in algal band width, community composition, and thallus colour along the canal (Upstream 0–184 km)

Supplementary Table 3

Month	Transparency (m)	Total radiation (W/m^2)	I_0 ($\mu mol\ m^{-2}\ s^{-1}$)	k (m^{-1})	Predicted depth (m)
Jan	2	119.48	245.71	0.85	1.31
Feb	2.5	152.33	313.27	0.68	1.99
Mar	4	187.39	385.37	0.425	3.67
Apr	4.5	240.88	495.37	0.378	4.79
May	2.2	250.23	514.59	0.773	2.39
Jun	3.6	216.63	445.49	0.472	3.61
Jul	4	247.35	508.67	0.425	4.32
Aug	3	185.58	381.64	0.567	2.74
Sep	2.5	113.43	233.27	0.68	1.56
Oct	2.5	78.53	161.5	0.68	1.01
Nov	2.2	108.53	223.19	0.773	1.31
Dec	1.5	113.63	233.68	1.133	0.93

Supplementary Table 3: Monthly transparency, incident radiation, light attenuation coefficient, and predicted optimal growth depth for *Cladophora.* I_0 represents the calculated surface irradiance converted from total radiation. The attenuation coefficient k was estimated from monthly transparency data. Predicted depth refers to the water depth at which underwater irradiance reaches 81 $\mu mol\ m^{-2}\ s^{-1}$, the irradiance threshold used for estimating the optimal growth depth of *Cladophora.*

Supplementary Fig. 13

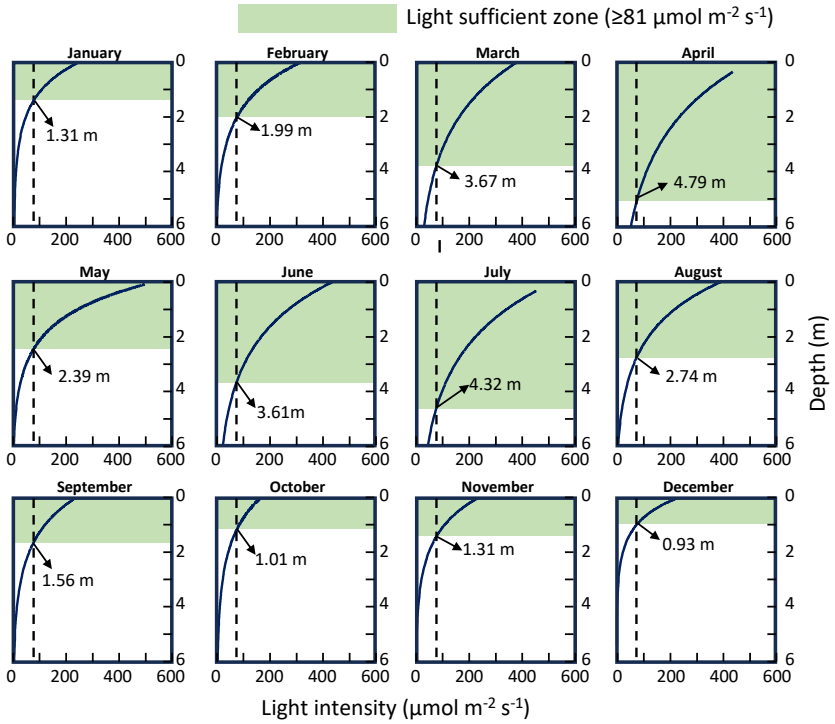

Supplementary Fig. 13: Predicted monthly optimal growth depth of *Cladophora* derived from transparency-controlled light attenuation. Depth-dependent irradiance profiles from January to December were calculated using the Lambert–Beer model with monthly transparency-derived attenuation coefficients and surface irradiance. The optimal growth depth was defined as the depth at which underwater irradiance reached 81 µmol m^{-2} s^{-1}, the experimentally determined optimal irradiance for *Cladophora* growth. The predicted optimal depth showed clear seasonal variation, reaching the deepest position in April at 4.79 m and remaining relatively deep in July at 4.32 m, corresponding to periods of higher water transparency and stronger light penetration. In winter, enhanced light attenuation compressed the optimal growth zone toward the surface, with the shallowest predicted depth occurring in December at approximately 0.93.